ACS Catalysis

pubs.acs.org/acscatalysis Research Article

# Functional Implications of Second-Shell Basic Residues for dUTPase DR2231 Enzymatic Specificity

Pietro Vidossich, Luis Eduardo Castañeda Moreno, Cristiano Mota, Daniele de Sanctis, Gian Pietro Miscione,* and Marco De Vivo*

Cite This: *ACS Catal.* 2020, 10, 13825−13833 Read Online

ACCESS | Metrics & More | Article Recommendations | Supporting Information

**ABSTRACT:** Nucleotide-processing enzymes are key players in biological processes. They often operate through high substrate specificity for catalysis. How such specificity is achieved is unclear. Here, we dealt with this question by investigating all-$\alpha$ dimeric deoxyuridine triphosphate nucleotidohydrolases (dUTPases). Typically, these dUTPases hydrolyze either dUTP or deoxyuridine diphosphate (dUDP) substrates. However, the dUTPase enzyme DR2231 from *Deinococcus radiodurans* selectively hydrolyzes dUTP only, and not dUDP. By means of extended classical molecular dynamics simulations and quantum chemical calculations, we show that DR2231 achieves this specificity for dUTP via second-shell basic residues that, together with the two catalytic magnesium ions, contribute to properly orienting the $\gamma$-phosphate of dUTP in a prereactive state. This allows a nucleophilic water to be correctly placed and activated in order to perform substrate hydrolysis. We show that this enzymatic mechanism is not viable when dUDP is bound to DR2231. Importantly, in several other dUTPases capable of hydrolyzing either dUTP or dUDP, we detected that active site second-shell basic residues are more in number, anchoring the $\beta$-phosphate of the nucleotide substrate too, in contrast to what is observed in DR2231. Thus, strategically located basic second-shell residues mediate precise reactant positioning at the catalytic site, determining substrate specificity in dUTPases and possibly in other structurally similar nucleotide-processing metalloenzymes.

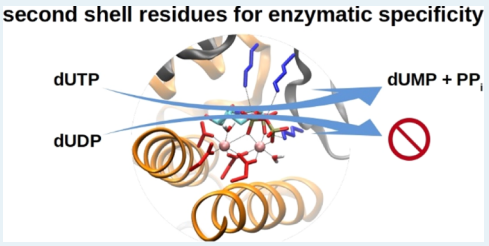


**KEYWORDS:** *enzyme specificity, nucleotide hydrolysis, two-metal-ion mechanism, molecular dynamics, quantum chemical cluster approach*



## INTRODUCTION

Nucleotide-processing enzymes are vital for biological processes such as cellular signaling, metabolism, and nucleic acid biosynthesis.[1,2] These enzymes are highly specialized, often functioning via high specificity for substrate (nucleotide) selection and hydrolysis.[3,4] However, there is poor understanding of the enzymatic strategy to attain this specificity for the elected substrate. Here, we analyze substrate specificity of all-$\alpha$ dimeric deoxyuridine triphosphate nucleotidohydrolases (dUTPases), a class of enzymes that hydrolyze uracil (U)-containing deoxynucleotides.[5] This hydrolytic action lowers the intracellular concentration of dUTP, limiting its incorporation into nascent DNA. dUTPases thus operate as essential house cleaners within the cell, as proved by dUTPase knockout experiments in *Escherichia coli* and yeast.[4] Notably, human dUTPase has been proposed as a promising drug target because its suppression sensitizes cancer cell lines to thymidylate synthase inhibition.[6] Furthermore, inhibition of trypanosomal dUTPases has been proposed as a therapeutic strategy for the treatment of neglected tropical diseases such as trypanosomiases and leishmaniasis.[7−9]

There are different superfamilies of dUTPases.[5,10] The all-$\alpha$ superfamily includes dUTPases that adopt the common two-metal-ion active site architecture for nucleic acid processing,[11] which usually promotes both dUTP and deoxyuridine diphosphate (dUDP) hydrolysis in these enzymes. This metal-aided enzymatic strategy is used to bring the reactants in contact and properly orient them for the activation of the nucleophilic water molecule, ultimately leading to substrate hydrolysis.[11−17]

Intriguingly, recent experimental data[18] have shown that the enzyme DR2231, a dimeric all-$\alpha$ dUTPase from *Deinococcus radiodurans*, selectively hydrolyzes only the dUTP substrate, in contrast to most members of the superfamily, which can unselectively hydrolyze both dUDP and dUTP.[10] However, given that experimental evidence suggests binding of dUDP to the active site,[18] DR2231's specificity for dUTP is mechanistically unexplained. The availability of structural and kinetics data on DR2231 catalysis[18,19] provides an optimal opportunity to dissect the fundamental aspects of the enzymatic processing of nucleotides by dUTPases.

Received: September 22, 2020
Revised: October 28, 2020




https://dx.doi.org/10.1021/acscatal.0c04148
*ACS Catal.* 2020, 10, 13825−13833

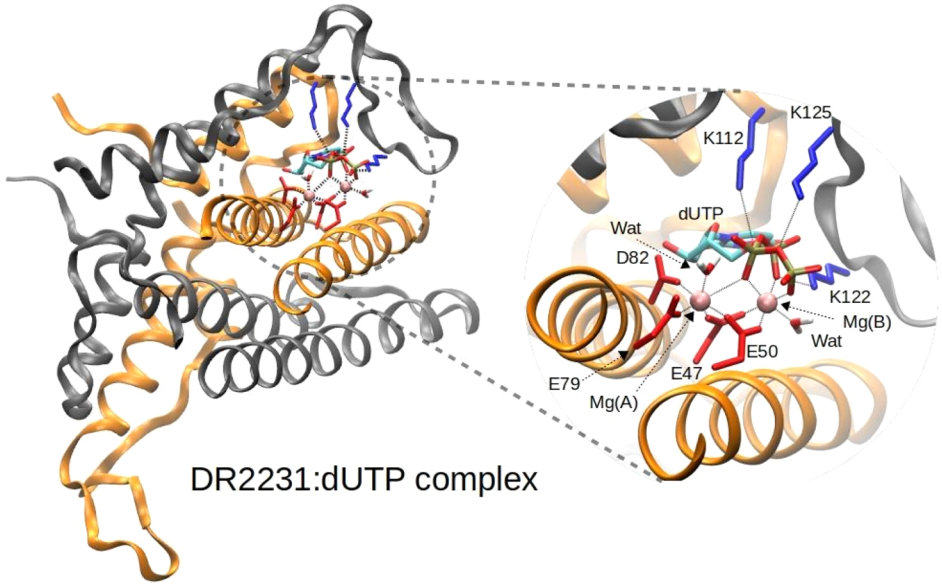


**Figure 1.** Model of DR2231 based on the crystallographic structure with PDB code: 5HVA.[18] The bound dUTP is modelled on the analog 2′-deoxyuridine 5′-$\alpha,\beta$-imido triphosphate. Acidic (Asp, Glu) and basic (Lys) residues interacting with substrate or the divalent cations are shown as red and blue sticks, respectively. Divalent magnesium cations are shown as pink spheres.

In detail, recent structural data have revealed the overall fold of DR2231,[19] which shares a common helix bundle with other dimeric dUTPases (Figure 1). This is used to hold in place the conserved catalytic two-metal-ion motif. The bimetallic catalytic center is surrounded by a number of second-shell positively charged residues, which are commonly found in the vicinity of the reactive site in nucleic-acid-processing enzymes.[13] Importantly, mutagenesis studies showed that such second-shell basic residues (namely, Lys112, Lys122, and Lys125) are required for efficient catalysis in DR2231.[18] These residues are involved in the interactions with the dUTP phosphate tail, although their exact functional contribution to catalysis is unclear. In addition, DR2231 and dimeric dUTPases bind the selected substrate in a dissimilar way. For DR2231, a mobile loop closes over the substrate. For dimeric dUTPases, a mobile $\alpha$-helical domain undergoes a conformational change upon ligand binding. However, it is unclear which structural features lead to efficient and selective catalysis in DR2231 versus other metal-dependent dUTPases.

Here, we integrate extended classical molecular dynamics (MD) simulations[20] of wild-type and mutated enzymatic forms of DR2231, quantum chemical calculations, and structural data analyses to identify the main determinants used by this enzyme to selectively process dUTP and not dUDP. We show that, together with the catalytic ions, specific second-shell basic residues in DR2231 contribute to properly orienting the $\gamma$-phosphate of the elected substrate dUTP at the catalytic site. In this way, the enzyme/dUTP complex is correctly assembled in a competent pre-reactive state for efficient and selective catalysis, allowing the correct placing and activation of the nucleophilic water for the substrate hydrolysis.

## RESULTS

**DR2231 Precatalytic Active Site State Forms Only when Bound to dUTP and Not to dUDP.** We performed extensive MD simulations to investigate the enzyme DR2231 in complex with either deoxyuridine triphosphate, dUTP, or deoxyuridine diphosphate, dUDP. Models were based on the X-ray structure of DR2231 in complex with a nonreactive dUTP analog (dUMPNPP, PDB code: 5HVA[18]). In this structure, the phosphate tail adopts two conformations with similar populations. In both cases, a water molecule is coordinated to Mg(A). Notably, this water is properly positioned for an in-line attack on the $\beta$-phosphate only in the most abundant conformation, which thus was used to model both dUTP/DR2231 and dUDP/DR2231 complexes (Figure 1).

The overall enzyme structure was well-maintained during the ∼500-ns-long MD simulations of the dUTP/DR2231 and dUDP/DR2231 complexes, showing very similar global structural properties (see Supporting Informations S1 and S2). In the MD simulation of the dUTP/DR2231 complex, four similar coordination patterns were observed for the two Mg ions (Figure 2 and S6), two of which (accounting for 34% of the simulated time) closely resemble the coordination of the catalytic Mg ions in the X-ray structure with PDB code:5HVA. In two of these coordination patterns, the position of the $\beta$-phosphate ($P_\beta$) changes from bridging Mg(A) and Mg(B) to coordinating Mg(B) only. In the remaining two coordination patterns, $P_\beta$ coordinates to Mg(B) and the coordination sphere of Mg(A) is completed by either a second water molecule or Glu79 in bidentate mode. Mg(A) coordination is thus more flexible, with ligand exchange events that involve solvent water or the oxygen atoms of $P_\beta$ and Glu79. Importantly, a water molecule is stably bound to Mg(A) throughout the simulations. This water is properly oriented for an in-line attack to the $P_\beta$ of dUTP. Furthermore, this water molecule is often H-bonded to one carboxylic oxygen of the nearby Glu79. We note that this glutamate may therefore serve as a proton acceptor during the nucleophilic attack. Also, three surrounding Lys residues interact with the phosphate tail. Specifically, Lys112 is stably engaged with $P_\alpha$ and $P_\beta$, while Lys122 is engaged with $P_\alpha$. Lys125 interacts with $P_\gamma$ and the oxygen bridging $P_\beta$ and $P_\gamma$ for most of the trajectory, occasionally breaking these interactions (Figure 3). Thus, overall, the active site geometry preserves a precatalytic state for dUTP


https://dx.doi.org/10.1021/acscatal.0c04148
ACS Catal. 2020, 10, 13825−13833

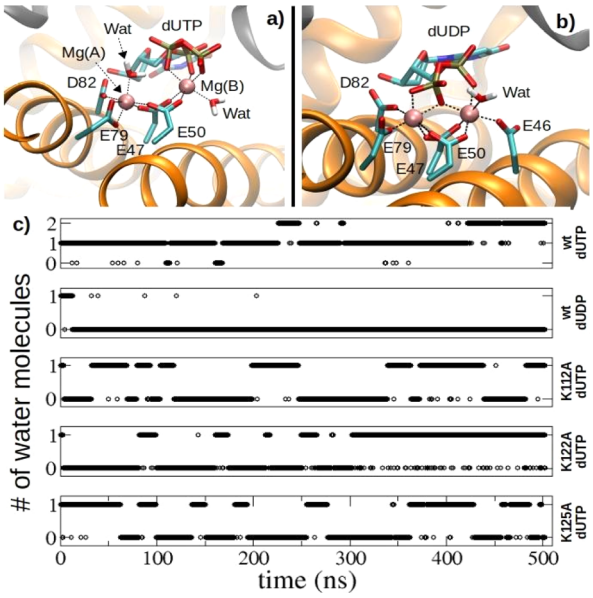


**Figure 2.** Representative conformations from the MD trajectories of the dUTP- (panel a) and dUDP-bound (panel b) DR2231 dUTPase (see the Supporting Information for further conformations from the cluster analysis of the respective trajectories). Panel c shows the number of water molecules bound to Mg(A) during the MD simulations of (top to bottom) wild-type DR2231 bound to dUTP and dUDP and K112A, K122A, and K125A mutants bound to dUTP.

hydrolysis, in accordance with the recognized two-metal-ion mechanism.[11]

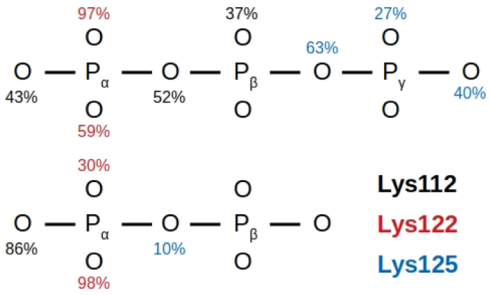


**Figure 3.** Interactions between the phosphate tails of dUTP and dUDP with Lys112 (black numbers), Lys122 (red), and Lys125 (blue) during the MD simulations. Reported are the percentages of structural snapshots from our trajectories in which a distance <3.5 Å was observed between the oxygen atom and side chain N atom of the Lys.

In contrast, in the dUDP/DR2231 complex, the nucleophilic water molecule unbinds irreversibly from Mg(A) in the early phases of the simulations. In fact, the clustering algorithm highlighted only two different Mg coordination patterns, neither of which features a water molecule bound to Mg(A) (Figure 2 and S6). In detail, $P_\beta$ rotates towards Mg(A), to which it binds with a second oxygen displacing the nucleophilic water molecule initially placed on the metal. Then, lack of $P_\gamma$ on dUDP frees a coordination site on Mg(B), which is immediately taken by a water molecule from the bulk. In turn, Glu46 displaces a water molecule and binds to Mg(B), occupying a position observed in the X-ray structure (PDB code: 5HVA) and possibly related to an alternative conformation of the phosphate tail, in which $P_\gamma$ is not bound to Mg(B). Notably, the interactions of the Lys residues with the phosphate tail of dUDP also rearrange significantly, strengthening the interactions with $P_\alpha$ and weakening those with the $P_\beta$ (Figure 3).

Taken together, the simulations suggest that the formation of a precatalytic state occurs via proper substrate positioning, which is only observed with dUTP at the catalytic site of DR2231.

We wanted to further test our hypothesis that nucleotide selectivity is mediated by the second-shell-residue-mediated proper positioning of the substrate, which allows nucleophile activation at the catalytic site. We therefore considered the DR2231 singularly mutated variants Lys112Ala, Lys122Ala, and Lys125Ala. These mutants display an experimental 100-fold reduction of the enzymatic activity.[18] We also performed ~500-ns-long MD simulations for each of these DR2231 variants bound to dUTP. Analysis of global structural parameters revealed that the mutations do not impact the fold (see the Supporting Information). However, formation of the precatalytic active site geometry is considerably reduced to about 50% in all of the variants, compared to the wild-type enzyme (Figure 2). In fact, for all three mutants, clustering analysis revealed two dominant states, both with a similar population, but characterized by a difference in the Mg(A) coordination shell (Figure S7). While one state shows the presence of the nucleophilic water properly coordinated to Mg(A), the other state does not feature such a nucleophilic water molecule bound to Mg(A). The lack of one of the second-shell residues Lys112, Lys122, or Lys125 and their interaction with the substrate (see paragraph above) strengthens the interaction between the oxygens at $P_\beta$ of dUTP and Mg(A). This, in turn, affects the coordination sphere of Mg(A), which does not include any water molecule when Glu79 binds in a bidentate mode. Simulations performed for the Lys112A, Lys122A, and Lys125A variants bound to dUDP are in line with these findings, showing essentially no binding of water molecules to Mg(A) (Figure S5). These results thus further support the functional implications of the basic second-shell residues Lys112, Lys122, or Lys125, explaining why these mutated DR2231 variants have reduced activity, given that all of them display reduced population of the precatalytic active site state.

**Enzymatic Mechanism for dUTP Hydrolysis in DR2231.** We furthered our understanding of dUTP hydrolysis in DR2231 with density functional theory (DFT) calculations, performed with the M06 functional[21] within the cluster approach[22] and taking solvation effects into account. In this way, we investigated the reaction mechanism for dUTP hydrolysis in DR2231 using a large model system, built from the X-ray structure (PDB code:5HVA). The model comprised the substrate and all of the water molecules (six) and amino acid residues within 8 Å of any substrate atom (252 atoms in total, Figure S9). The optimized structure (**I1**, Figure S10) closely resembles the starting X-ray structure (rmsd = 0.99 Å). The nucleophilic water ($Wat_{Cat}$, hereafter), coordinated to Mg(A), forms a stable H-bond with Glu79 (O4−H1 = 1.69 Å) and another water molecule, which in turn is interacting with O3 of the $\gamma$-phosphate. This H-bond network suggests that alternative reaction pathways can originate from **I1**, differing in the mode in which the nucleophilic water is activated (i.e., deprotonated).

In mechanism A (critical points and energy profile shown in Scheme 1), Glu79 directly deprotonates $Wat_{Cat}$. Interestingly,


https://dx.doi.org/10.1021/acscatal.0c04148
ACS Catal. 2020, 10, 13825−13833

**Scheme 1. Schematic Representation of the Structures of Critical Points I1, TS1_A, I2, TS2_A, and I3_A of Mechanism A and Relative Energy Profile (Bottom Right)**[a]

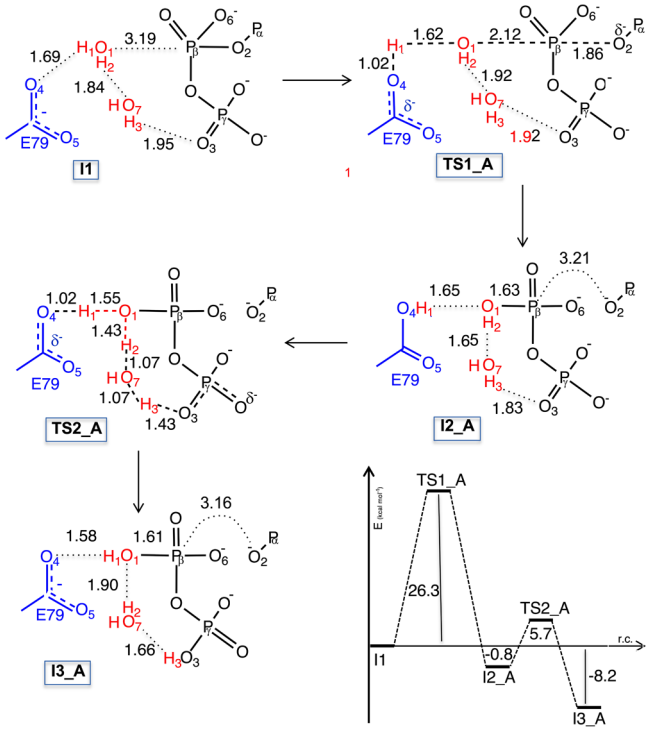


[a]Because we adopted a 2D representation, some atomic distances may not be realistic and may appear much longer or shorter than in the true system (distances are reported in angstroms).

we could not locate any intermediate featuring a protonated Glu79 and a deprotonated water still coordinated to Mg(A). This reflects the fact that water activation and nucleophilic attack are concerted chemical events. However, as the **TS1_A** transition state geometry (Figure S11) indicates, water activation and nucleophilic attack are asynchronous: while water deprotonation is fully completed (O4−H1 = 1.02 Å), the phosphoryl transfer reaction is still in progress, with the forming ($P_\beta$-O1) and breaking ($P_\beta$-O2) bonds of 2.12 and 1.86 Å length, respectively. Notably, the hydrogen bond network involving the nucleophile and the leaving group (H-bonded to Lys125) seems to be important for the correct positioning and activation of the reacting species. In particular, each of the three second-shell lysine residues (Lys112, Lys122, and Lys125) is interacting through hydrogen bonds with different oxygen atoms of the pyrophosphate leaving group (Figure S11). Indeed, the nucleophile, the electrophilic center, and the leaving group are almost perfectly aligned (the O1-$P_\beta$-O2 angle is 176°), as demanded in an ideal $S_N2$ mechanism. These structural features emphasize the role of the enzyme and the metal co-factors in correctly positioning the reactive species to catalyze the reaction process.

**TS1_A** lies 26.3 kcal mol$^{-1}$ above **I1**. In the following intermediate (I2_A, 0.8 kcal mol$^{-1}$ more stable than **I1**), Glu79 is protonated, the O1-$P_\beta$ bond is formed (1.63 Å), and $P_\beta$-O2 is broken (3.21 Å). Then, the last examined step is the regeneration of the enzyme initial state, which occurs through a triple concerted proton transfer, involving a second water molecule and the substrate (**TS2_A**, 5.7 kcal mol$^{-1}$ above **I1**). The net result is the deprotonation of Glu79 in favor of the $\gamma$-phosphate of the leaving substrate. In this way, the enzyme returns in its initial catalytic state (intermediate **I3_A**, 8.2 kcal mol$^{-1}$ below **I1**).

The activation and the nucleophilic attack of the catalytic water occur in the same kinetic step also in mechanism B (see Figure S12). However, in this case the deprotonation of the catalytic water is carried out by the substrate $\gamma$-phosphate through a bridging, crystallographic water molecule, without the direct intervention of Glu79. Thus, in mechanism B the reaction is substrate-assisted. In the rate-determining step (TS1_B, 27.9 kcal mol$^{-1}$ above **I1**), as the catalytic water is attacking the $\beta$-phosphate (O1-$P_\beta$ = 1.90 Å), two proton transfers occur simultaneously: H2 is hopping from O1 of the catalytic water to O7 of the bridging water (H2−O1 = 1.18 Å, H2−O7 = 1.24 Å), which, in turn, is passing H3 to O3 of the substrate $\gamma$-phosphate. The role of Glu79 is to assist the nucleophile attack through a hydrogen bond with the catalytic water (H1−O4 = 2.59 Å in TS1_B). The net result is the deprotonation of the attacking catalytic water, which leads to **I3_A**, as already discussed in mechanism A. To explore further reaction mechanisms, we also considered an alternative way for the activation of $Wat_{Cat}$. In this pathway (mechanism C, Figure S13), the proton shuttle needed to activate $Wat_{Cat}$ and transfer the migrating proton to Glu79, is mediated by the same bridging water used in mechanism B. However, here the double proton hopping occurs prior to the nucleophilic attack, yielding an intermediate featuring $Wat_{Cat}$ as an activated hydroxide. Then, the hydroxide can proceed and perform the phosphoryl transfer reaction, as described in more detail in the Supporting Information, although this route is unfavored based on energy grounds. We also considered the possibility of a water molecule not bound to Mg(A) attacking the $\beta$-phosphate, which however turned to be energetically too demanding (Figure S14), in line with previous results on phosphate hydrolysis in solution.[23,24] Overall, our mechanistic study suggests mechanism A as the most favored reaction pathway for dUTP hydrolysis in DR2231.

We further assessed the stabilizing effect of the three second-shell lysine residues (Lys112, Lys122, and Lys125) on the rate-determining step energy barrier of mechanism A. To this aim, we carried out single-point energy calculations including solvation effects on **I1** and **TS1_A** removing all, and also one at a time, the lysine residues. The calculated energy barrier of the system including all of the lysine residues is 26.3 kcal mol$^{-1}$. This value increased to 41.5 kcal mol$^{-1}$ when all of the lysine residues were removed and to 32.0, 31.3 and 31.7 kcal mol$^{-1}$ when Lys112, Lys 122 or Lys125 were not present, respectively. Thus, our calculations indicate that all of the lysine residues have a catalytic (and synergistic) effect on the **TS1_A** stabilization.

## DISCUSSION

In this study, we have used classical and quantum modeling to understand the molecular determinants for specificity in hydrolytic enzymes.[25−27] In particular, we used all-atom force-field-based MD and DFT-based quantum mechanical calculations to investigate the determinants for substrate specificity attained by the enzyme DR2231, which belongs to the all-$\alpha$ dimeric deoxyuridine triphosphate nucleotidohydrolases (dUTPases) family.[10] Intriguingly, the enzyme DR2231 hydrolyzes only dUTP.[18] This is in contrast to other members of the all-$\alpha$ dimeric dUTPases family, which hydrolyze both dUTP and dUDP.[10] Clarifying how DR2231 specifically


https://dx.doi.org/10.1021/acscatal.0c04148
ACS Catal. 2020, 10, 13825−13833

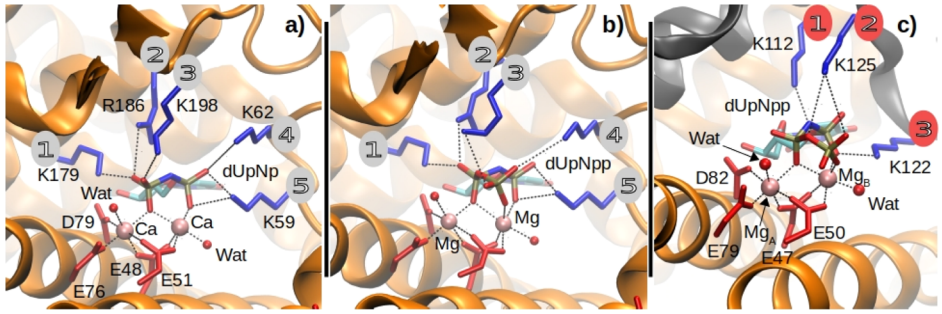


**Figure 4.** Active site of dimeric dUTPase from *L. major* in complex with dUDP (dUpNP) and dUTP (dUpNpp) analogs[33] (panels a and b, respectively), and of DR2231 from *D. radiodurans* in complex with dUTP analog[18] (panel c). Some structural studies were performed with divalent cations other than $Mg^{2+}$ (e.g., $Ca^{2+}$, $Mn^{2+}$), which, however, are considered not catalytically competent at physiological conditions.

cleaves dUTP only may help in understanding the mechanistic strategy used by nucleotide-processing enzymes to achieve substrate selectivity.

First, we used MD equilibrium simulations to analyze multiple systems of DR2231 in complex with dUTP or dUDP. We found that the precatalytic state of the active site in DR2231 forms only when the enzyme is bound to dUTP, and not to dUDP. This was shown by the stability of the active site of the dUTP/DR2231 complex, which maintained a water molecule bound to Mg(A) and optimally located to perform nucleophilic attack at the $P_\beta$ on dUTP. Importantly, we noted that this precatalytic state was formed thanks to the cooperative action of three second-shell lysine residues (Lys112, Lys122, and Lys125). These lysines, together with Mg(B),[18] act by securing $P_\alpha$ and $P_\gamma$ in their bound location. In this way, in our MD simulations, the reactants form a stable Michaelis complex that is ready for catalysis. Here, the nucleophile activation is possible by proper substrate positioning, with the nearby Glu79 well-positioned to facilitate water deprotonation and activation, thus favoring the ensuing phosphoryl transfer reaction.[11,12,14]

These results differ to what we observed in our MD simulations of the dUDP/DR2231 complex, where the three key second-shell lysines (Lys112A, Lys122, and Lys125) are not sufficient to guarantee formation of the Michaelis complex. Consequently, $P_\beta$ of dUDP is loose and free to coordinate to Mg(A), displacing the nucleophilic water molecule, located at the catalytic site at the beginning of the simulation. These findings suggest that catalysis in DR2231 occurs via nucleophile activation by proper substrate positioning, which is only allowed in the case of the substrate dUTP, thanks to the specific action of Mg(B) and the three second-shell lysine residues, which are thus key for function.[13,28]

Then, upon proper Michaelis complex formation, we used DFT calculations to show that catalysis can proceed through a typical $S_N2$ reaction mechanism in which Glu79 acts as a general base. Glu79 can accept a proton from the nucleophilic water, which is thus activated to perform phosphoryl transfer and hydrolyze dUTP. Water activation and dUTP hydrolysis appear concerted and asynchronous, with a computed energy barrier of 26.3 kcal $mol^{-1}$ (vs the estimated value of 16.6 kcal $mol^{-1}$ calculated from the experimental[19] $k_{cat}$ using the Eyring−Polanyi equation). The discrepancy between the computational and experimental estimates of the activation free energy barrier may be due to several factors: (i) the size of the model system considered—about 250 atoms, which is a subset of the full enzyme, and thus may not include catalytic long range electrostatic effects; (ii) the limited flexibility allowed to the cluster model—fluctuations may considerably affect the size of enzymatic barriers,[29] especially when proton transfers are involved; (iii) the accuracy of the level of theory—here DFT in the M06 form, which although demonstrating a good general accuracy,[21] is not tailored to the system and chemistry investigated here.[30]

Taken together, our results suggest an enzymatic strategy where correct substrate positioning at the catalytic site in DR2231 is mediated by the metal ions[18] and, crucially, by three positively charged second-shell residues. Together, this concerted action allows prompt nucleophile activation (through Mg(A) and Glu79), followed by phosphoryl transfer via the recognized two-metal-ion mechanism.[11,12,14]

Interestingly, further analyses of the available X-ray structures of all-$\alpha$ dimeric dUTPases from other organisms (namely, from *Trypanosoma cruzi*,[31] *T. brucei*,[32] *Leishmania* major,[33] and *Campylobacter jejuni*[34]) reveal that all-$\alpha$ dimeric dUTPases can indeed form a precatalytic state with both dUTP and dUDP. We noted that, in the all-$\alpha$ dimeric dUTPases, the phosphate tail of either substrates dUTP or dUDP is anchored by 5 positively charged residues (as in *Leishmania* major dUTPase,[33] where dUTP is in close contact with Lys179, Arg186, Lys 198, Lys59, and Lys62, Figure 4). In this case, two (for dUTP) or three (for dUDP) conserved basic residues secure the $\beta$-phosphate at the catalytic site (see the Supporting Information). However, in DR2231, the tail of the processed substrate dUTP interacts with three lysine residues (Lys112, Lys122, and Lys125, Figure 4). Here, Lys112 and Lys122 interact with the $\alpha$-phosphate, while Lys125 is about 4 Å from the $\gamma$-phosphate. Notably, when Lys112, Lys122, or Lys125 is mutated to Ala, processing of dUTP by DR2231 is substantially diminished.[18] It thus appears that these second-shell basic residues are crucial for enzymatic specificity. Importantly, this is in line with our MD simulations of the Lys112Ala, Lys122Ala, and Lys125Ala variants in complex with dUTP. Our simulations revealed that the population of the precatalytic state is reduced for these variant forms of DR2231 relative to wild type. This is because the $\beta$-phosphate in these variants is now capable of displacing the nucleophilic water from $Mg_A$, thus hampering catalysis.

Taken together, our results and structural observations further reinforce a recent proposal on the importance of positively charged second-shell residues in two-metal-ion nucleic-acid-processing enzymes (second shell with respect to the metal ions, but in direct contact with the substrate).[13] Previous structural alignments revealed that basic residues and cations occupy conserved positions surrounding the active site of two-metal-ion polymerases, nucleases, and ribozymes.[13] In


https://dx.doi.org/10.1021/acscatal.0c04148
ACS Catal. 2020, 10, 13825−13833

line with this evidence, here we show that strategically located second-shell lysine residues may indeed be functional, as in this case, where they help dictate the specificity of dUTPases by controlling the positioning of the phosphate tail of the substrate, which in turns favors nucleophile activation for catalysis.

## CONCLUSIONS

In this study, we addressed the origin of substrate specificity in the dUTPase DR2231, which hydrolyzes dUTP but not dUDP. This is in contrast to other members of the all-$\alpha$ dimeric dUTPase family, which process both dUTP and dUDP nucleotides. Based on MD simulations and DFT-based calculations, we showed that DR2231 attains specificity for dUTP via the proper assembly of the reactants at the active site. The dUTP phosphate tail is anchored in a prereactive state by Mg(B) and by second-shell basic residues, which are critical to properly orienting the substrate for its hydrolysis. In this conformational state, the nucleophilic water is correctly placed to be deprotonated and perform substrate hydrolysis, as indicated by our DFT calculations. Importantly, this enzymatic mechanism is not feasible when dUDP is bound to DR2231 because then the three second-shell basic residues cannot interact with the missing $\gamma$-phosphate in dUDP. This second-shell basic-residue-mediated catalytic strategy for substrate selection in dUTPases is likely extendable to other structurally similar nucleotide-processing metalloenzymes capable of hydrolyzing both dUTP and dUDP, as revealed by our analysis of available X-ray structures of all-$\alpha$ dimeric dUTPases. Intriguingly, there are several other structurally similar nucleotide-processing metalloenzymes where second-shell residues are present at the catalytic site,[13] which may thus operate with a similar enzymatic strategy mediated by second-shell basic residues to attain specific substrate processing.

## METHODS

**Structural Analysis.** Dimeric dUTPases have been proposed as potential targets for drug design[6] and have thus been the object of a structural determination effort. Structures of dimeric dUTPases from *T. cruzi*,[31] *T. brucei*,[32] *L. major*,[33] and *C. jejuni*[34] have been determined under diverse conditions and with different ligands. Of the available structures, here we considered those of wild-type enzymes in complex with dUTP or dUDP substrate analogs and with both divalent ions bound at the active site. Specifically, the following structures were analyzed in this study (PDB codes and resolution in parentheses): 5HVA (2.10 Å resolution), 4DKB (1.83 Å), 4DLC (1.76 Å), 2YAY (1.86 Å), 2CJE (2.341.8 Å), 2CIC (1.70 Å), and 1W2Y (1.65 Å). Relevant features of these structures are described in the Supporting Information.

**MD Simulations.** To investigate the functional dynamics of the dUTPase DR2231 complex, we employed extensive force-field-based MD simulations, as previously used in several informative studies on metal-aided enzymatic complexes dealing with nucleotides and nucleic acids.[35−39] Here, model systems for the classical MD simulations were based on the X-ray structure of DR2231 in complex with a substrate analog and magnesium (PDB code:5HVA[18]). Chains A and C of the PDB file 5HVA were used. The missing residues Pro116-Leu124 in chain C were reconstructed with the ModLoop web server (https://modbase.compbio.ucsf.edu/modloop).[40] The N- and C-termini of the polypeptide chains were saturated with acetyl and N-methyl groups. The substrate analog was modified to dUTP. Asp, Glu, Arg, and Lys residues were assumed in their charged state and His uncharged, as estimated using PROPKA.[41] Specifically, His15, 57, and 106 were protonated at the $N_\varepsilon$, whereas His18, 78, and 143 were protonated at the $N_\delta$ based on visual inspection of the local environment. About 25,000 water molecules were used to solvate the protein. The number of Na cations and Cl anions was adjusted to neutralize the simulation cell and to reach concentrations around 100 mM. Simulations were performed for the wild-type enzyme bound to dUDP and dUTP, and for the variants Lys112Ala, Lys122Ala, and Lys125Ala bound to dUTP and dUDP.

The following force fields were used: the AMBER ff14SB for protein,[42] TIP3P for water,[43] Joung and Cheatham for Na and Cl ions,[44] and Li et al. for Mg ions.[45] Bonding parameters from the General Amber Force Field[46] were used for dUTP and dUDP. Point charges for dUTP and dUTP were developed according to the RESP methodology based on a fragment approach.[47] Specifically, charges were derived separately for the triphosphate and disphosphate moieties and for the nucleoside.

MD simulations were performed with the GPU version of the PMEMD code of the AMBER package.[48,49] The system was treated under periodic boundary conditions. Simulation cells were cubic of about 93 Å edge. Long-range electrostatic interactions were treated with the PME method.[50] A 10 Å cutoff was used for the real part of the electrostatic and for van der Waals interactions. The integration time step was 2 fs. SHAKE was used to constrain bonds involving hydrogen atoms.[51] Simulations were performed at constant temperature (310 K) and pressure (1 bar). After 2 ns of solvent equilibration and energy minimization, the system was gradually heated to 310 K in 2.5 ns, maintaining the protein backbone close to the crystallographic positions by applying a soft harmonic potential. Then, 500 ns of production MD were performed. Analysis of the MD trajectory was based on the calculation of structural descriptors: the root-mean-square deviation (rmsd) with respect to the initial structure for the protein backbone atoms and the backbone atoms of secondary structure elements; the radius of gyration of the backbone atoms; the root mean square fluctuations (rmsf) of the $C_\alpha$ atoms. A clustering analysis based on the density of data points was performed.[52] The distance between data points was measured by the rmsd of the coordinates of Mg ions and the oxygen atoms of Glu186, Glu189, Glu218, Asp221, and the di/triphosphate moiety. Structures for every 20 ps of simulation were used in the analysis.

**Quantum Chemical Calculations.** A cluster model[53] of the active site was constructed from the PDB structure file 5HVA. The cluster comprised the substrate and all of the water molecules and amino acid residues found at a distance less than 8 Å from any substrate atom. All of the amino acids directly interacting with the substrate were included, plus other nearby residues. To reduce the system size and simulate the static nature of the enzyme backbone, the backbone carbon atoms were replaced by hydrogen atoms, which were kept fixed during geometry optimization (17 H atoms). Hydrogen atoms were added manually. Protonation states of ionizable amino acids were consistent with the model used for the MD simulations.

All reported DFT computations were executed with the Gaussian16 series of programs.[54] See, for example, ref 30 for a


https://dx.doi.org/10.1021/acscatal.0c04148
ACS Catal. 2020, 10, 13825−13833

benchmark of the performance of different DFT functionals for the hydrolysis of phosphodiester bonds. Here, because the investigated model system also contains aromatic groups and metal ligands, a trustworthy evaluation of noncovalent interactions involving $\pi$ systems and metal coordination is essential in computing the potential energy surface. Thus, we chose the M06 functional,[21] which is capable of treating metals, noncovalent interactions, and medium−range correlation effects. We performed geometry optimization calculations using two basis sets: the 6-31+G* basis set[55] for the substrate molecule and the atoms closer to the reaction center (59 atoms) and the 3-21G* basis set[56] for the remaining 193 atoms. For each stationary point, we performed harmonic vibrational frequencies computations to determine their nature and to obtain zero-point energies. Successively, we run single-point energy calculations on the previously optimized geometries, using the 6-311+G(2d,2p) basis set on all atoms and including solvation effects with the SMD variation of IEFPCM of Truhlar and workers (SMD option in Gaussian 16).[57] A value of 4 was employed for the dielectric constant $\varepsilon$. All of the reported energy values refer to the sum of energies obtained through the solvation calculations and the corresponding zero-point energies.

## ■ ASSOCIATED CONTENT

### Supporting Information

The Supporting Information is available free of charge at https://pubs.acs.org/doi/10.1021/acscatal.0c04148.

Analysis of dimeric dUTPases structures; analysis of MD trajectories; analysis of alternative reaction mechanisms; and cartesian coordinates of all of the discussed critical points (PDF)

## ■ AUTHOR INFORMATION


### Corresponding Authors

**Gian Pietro Miscione** − *COBO Computational Bio-Organic Chemistry Bogotá, Chemistry Department, Universidad de Los Andes, 111711 Bogotá, Colombia;* orcid.org/0000-0003-2262-9179; Email: gp.miscione57@uniandes.edu.co

**Marco De Vivo** − *Molecular Modeling and Drug Discovery Lab, Istituto Italiano di Tecnologia, 16163 Genova, Italy;* orcid.org/0000-0003-4022-5661; Email: marco.devivo@iit.it

### Authors

**Pietro Vidossich** − *COBO Computational Bio-Organic Chemistry Bogotá, Chemistry Department, Universidad de Los Andes, 111711 Bogotá, Colombia; Molecular Modeling and Drug Discovery Lab, Istituto Italiano di Tecnologia, 16163 Genova, Italy*

**Luis Eduardo Castañeda Moreno** − *COBO Computational Bio-Organic Chemistry Bogotá, Chemistry Department, Universidad de Los Andes, 111711 Bogotá, Colombia*

**Cristiano Mota** − *ESRF The European Synchrotron, 38042 Grenoble Cedex 9, France*

**Daniele de Sanctis** − *ESRF The European Synchrotron, 38042 Grenoble Cedex 9, France*

Complete contact information is available at: https://pubs.acs.org/10.1021/acscatal.0c04148


### Notes

The authors declare no competing financial interest.

## ■ ACKNOWLEDGMENTS

G.P.M. acknowledges the High-Performance Computing Center of the Universidad de los Andes, Bogotá (Colombia), for the computational resources and the "Fondo de Apoyo para Profesores Asistentes" of the same institution for financial support. M.D.V. thanks the Italian Association for Cancer Research (AIRC) for financial support (IG 23679). C.M. acknowledges the "Fundação para a Ciência e Tecnologia" for a postdoctoral contract SFRH/BEST/51724/2011. D.d.S. and C.M. thank the PHC PESSOA 2016 (35797UH) Programme and the ESRF Structural Biology Group for support. P.V. and M.D.V. acknowledge the CINECA award under the ISCRA initiative (project id: HP10CNJ2TZ), for the availability of high performance computing resources and support.

## ■ REFERENCES


(1) Alberts, B.; Johnson, A.; Lewis, J.; Morgan, D.; Raff, M.; Roberts, K.; Walter, P. *Molecular Biology of the Cell*, 6th ed.; Garland Science, Taylor & Francis: New York, 2015; pp 1−1342.

(2) Kamerlin, S. C. L.; Sharma, P. K.; Prasad, R. B.; Warshel, A. Why Nature Really Chose Phosphate. *Q. Rev. Biophys.* **2013**, *46*, 1−132.

(3) Bourne, H. R.; Sanders, D. A.; McCormick, F. The GTPase Superfamily: Conserved Structure and Molecular Mechanism. *Nature* **1991**, *349*, 117−127.

(4) Vértessy, B. G.; Tóth, J. Keeping Uracil Out of DNA: Physiological Role, Structure and Catalytic Mechanism of dUTPases. *Acc. Chem. Res.* **2009**, *42*, 97−106.

(5) Galperin, M. Y.; Moroz, O. V.; Wilson, K. S.; Murzin, A. G. House Cleaning, a Part of Good Housekeeping. *Mol. Microbiol.* **2006**, *59*, 5−19.

(6) Koehler, S. E.; Ladner, R. D. Small Interfering RNA-mediated Suppression of dUTPase Sensitizes Cancer Cell Lines to Thymidylate Synthase Inhibition. *Mol. Pharmacol.* **2004**, *66*, 620−626.

(7) Hidalgo-Zarco, F.; Gonzalez-pacnowska, D. Trypanosomal dUTPases as Potential Targets for Drug Design. *Curr. Protein Pept. Sci.* **2001**, *2*, 389−397.

(8) Paulino, M.; Iribarne, F.; Dubin, M.; Aguilera-Morales, S.; Tapia, O.; Stoppani, A. The Chemotherapy of Chagas' Disease: An Overview. *Mini Rev. Med. Chem.* **2005**, *5*, 499−519.

(9) Riccardi, L.; Genna, V.; De Vivo, M. Metal-ligand Interactions in Drug Design. *Nat. Rev. Chem.* **2018**, *2*, 100−112.

(10) Moroz, O. V.; Murzin, A. G.; Makarova, K. S.; Koonin, E. V.; Wilson, K. S.; Galperin, M. Y. Dimeric dUTPases, HisE, and MazG Belong to a New Superfamily of all-alpha NTP Pyrophosphohydrolases with Potential "House-Cleaning" Functions. *J. Mol. Biol.* **2005**, *347*, 243−255.

(11) Palermo, G.; Cavalli, A.; Klein, M. L.; Alfonso-Prieto, M.; Dal Peraro, M.; De Vivo, M. Catalytic Metal Ions and Enzymatic Processing of DNA and RNA. *Acc. Chem. Res.* **2015**, *48*, 220−228.

(12) Steitz, T. A.; Steitz, J. A. A General 2-Metal-Ion Mechanism for Catalytic RNA. *Proc. Natl. Acad. Sci. U.S.A.* **1993**, *90*, 6498−6502.

(13) Genna, V.; Colombo, M.; De Vivo, M.; Marcia, M. Second-Shell Basic Residues Expand the Two-Metal-Ion Architecture of DNA and RNA Processing Enzymes. *Structure* **2018**, *26*, 40.

(14) Genna, V.; Donati, E.; De Vivo, M. The Catalytic Mechanism of DNA and RNA Polymerases. *ACS Catal.* **2018**, *8*, 11103−11118.

(15) Genna, V.; Gaspari, R.; Dal Peraro, M.; De Vivo, M. Cooperative Motion of a Key Positively Charged Residue and Metal Ions for DNA Replication Catalyzed by Human DNA Polymerase-eta. *Nucleic Acids Res.* **2016**, *44*, 2827−2836.

(16) Genna, V.; Vidossich, P.; Ippoliti, E.; Carloni, P.; De Vivo, M. A Self-Activated Mechanism for Nucleic Acid Polymerization Catalyzed by DNA/RNA Polymerases. *J. Am. Chem. Soc.* **2016**, *138*, 14592−14598.

(17) Palermo, G.; Stenta, M.; Cavalli, A.; Dal Peraro, M.; De Vivo, M. Molecular Simulations Highlight the Role of Metals in Catalysis

and Inhibition of Type II Topoisomerase. *J. Chem. Theory Comput.* **2013**, *9*, 857−862.
(18) Mota, C. S.; Gonçalves, A. M. D.; de Sanctis, D. Deinococcus radiodurans DR2231 is a Two-Metal-ion Mechanism Hydrolase with Exclusive Activity on dUTP. *FEBS J.* **2016**, *283*, 4274−4290.
(19) Gonçalves, A. M. D.; de Sanctis, D.; McSweeney, S. M. Structural and Functional Insights into DR2231 Protein, the MazG-like Nucleoside Triphosphate Pyrophosphohydrolase from Deinococcus radiodurans. *J. Biol. Chem.* **2011**, *286*, 30691−30705.
(20) De Vivo, M.; Masetti, M.; Bottegoni, G.; Cavalli, A. Role of Molecular Dynamics and Related Methods in Drug Discovery. *J. Med. Chem.* **2016**, *59*, 4035−4061.
(21) Zhao, Y.; Truhlar, D. G. The M06 Suite of Density Functionals for Main Group Thermochemistry, Thermochemical Kinetics, Noncovalent Interactions, Excited States, and Transition Elements: Two New Functionals and Systematic Testing of Four M06-class Functionals and 12 Other Functionals. *Theor. Chem. Acc.* **2008**, *120*, 215−241.
(22) Siegbahn, P. E. M.; Himo, F. The Quantum Chemical Cluster Approach for Modeling Enzyme Reactions. *Wiley Interdiscip. Rev.: Comput. Mol. Sci.* **2011**, *1*, 323−336.
(23) Akola, J.; Jones, R. O. ATP Hydrolysis in Water − A Density Functional Study. *J. Phys. Chem. B* **2003**, *107*, 11774−11783.
(24) Florián, J.; Warshel, A. Phosphate Ester Hydrolysis in Aqueous Solution: Associative versus Dissociative Mechanisms. *J. Phys. Chem. B* **1998**, *102*, 719−734.
(25) Biarnés, X.; Ardèvol, A.; Iglesias-Fernández, J.; Planas, A.; Rovira, C. Catalytic Itinerary in 1,3-1,4-beta-Glucanase Unraveled by QM/MM Metadynamics. Charge Is Not Yet Fully Developed at the Oxocarbenium Ion-like Transition State. *J. Am. Chem. Soc.* **2011**, *133*, 20301−20309.
(26) Liao, R.-Z.; Yu, J.-G.; Himo, F. Phosphate Mono- and Diesterase Activities of the Trinuclear Zinc Enzyme Nuclease P1-Insights from Quantum Chemical Calculations. *Inorg. Chem.* **2010**, *49*, 6883−6888.
(27) Hong, R.; Magistrato, A.; Carloni, P. Anthrax Lethal Factor Investigated by Molecular Simulations. *J. Chem. Theory Comput.* **2008**, *4*, 1745−1756.
(28) Genna, V.; Carloni, P.; De Vivo, M. A Strategically Located Arg/Lys Residue Promotes Correct Base Paring During Nucleic Acid Biosynthesis in Polymerases. *J. Am. Chem. Soc.* **2018**, *140*, 3312−3321.
(29) Ribeiro, A. J. M.; Santos-Martins, D.; Russo, N.; Ramos, M. J.; Fernandes, P. A. Enzymatic Flexibility and Reaction Rate: A QM/MM Study of HIV-1 Protease. *ACS Catal.* **2015**, *5*, 5617−5626.
(30) Ribeiro, A. J. M.; Ramos, M. J.; Fernandes, P. A. Benchmarking of DFT Functionals for the Hydrolysis of Phosphodiester Bonds. *J. Chem. Theory Comput.* **2010**, *6*, 2281−2292.
(31) Harkiolaki, M.; Dodson, E. J.; Bernier-Villamor, V.; Turkenburg, J. P.; González-Pacanowska, D.; Wilson, K. S. The Crystal Structure of Trypanosoma cruzi dUTPase Reveals a Novel dUTP/dUDP Binding Fold. *Structure* **2004**, *12*, 41−53.
(32) Hemsworth, G. R.; González-Pacanowska, D.; Wilson, K. S. On the Catalytic Mechanism of Dimeric dUTPases. *Biochem. J.* **2013**, *456*, 81−88.
(33) Hemsworth, G. R.; Moroz, O. V.; Fogg, M. J.; Scott, B.; Bosch-Navarrete, C.; Gonzalez-Pacanowska, D.; Wilson, K. S. The Crystal Structure of the Leishmania major Deoxyuridine Triphosphate Nucleotidohydrolase in Complex with Nucleotide Analogues, dUMP, and Deoxyuridine. *J. Biol. Chem.* **2011**, *286*, 16470.
(34) Moroz, O. V.; Harkiolaki, M.; Galperin, M. Y.; Vagin, A. A.; González-Pacanowska, D.; Wilson, K. S. The Crystal Structure of a Complex of Campylobacter jejuni dUTPase with Substrate Analogue Sheds Light on the Mechanism and Suggests the "Basic Module" for Dimeric d(C/U)TPases. *J. Mol. Biol.* **2004**, *342*, 1583−1597.
(35) Casalino, L.; Palermo, G.; Spinello, A.; Rothlisberger, U.; Magistrato, A. All-atom Simulations Disentangle the Functional Dynamics Underlying Gene Maturation in the Intron Lariat Spliceosome. *Proc. Natl. Acad. Sci. U.S.A.* **2018**, *115*, 6584−6589.
(36) Ho, M.-H.; De Vivo, M.; Dal Peraro, M.; Klein, M. L. Understanding the Effect of Magnesium Ion Concentration on the Catalytic Activity of Ribonuclease H through Computation: Does a Third Metal Binding Site Modulate Endonuclease Catalysis? *J. Am. Chem. Soc.* **2010**, *132*, 13702−13712.
(37) Yan, C.; Dodd, T.; He, Y.; Tainer, J. A.; Tsutakawa, S. E.; Ivanov, I. Transcription Preinitiation Complex Structure and Dynamics Provide Insight into Genetic Diseases. *Nat. Struct. Mol. Biol.* **2019**, *26*, 397.
(38) Donati, E.; Genna, V.; De Vivo, M. Recruiting Mechanism and Functional Role of a Third Metal Ion in the Enzymatic Activity of 5 ' Structure-Specific Nucleases. *J. Am. Chem. Soc.* **2020**, *142*, 2823−2834.
(39) Genna, V.; Marcia, M.; De Vivo, M. A Transient and Flexible Cation-pi Interaction Promotes Hydrolysis of Nucleic Acids in DNA and RNA Nucleases. *J. Am. Chem. Soc.* **2019**, *141*, 10770−10776.
(40) Fiser, A.; Sali, A. ModLoop: Automated Modeling of Loops in Protein Structures. *Bioinformatics* **2003**, *19*, 2500−2501.
(41) Olsson, M. H. M.; Søndergaard, C. R.; Rostkowski, M.; Jensen, J. H. PROPKA3: Consistent Treatment of Internal and Surface Residues in Empirical pK(a) Predictions. *J. Chem. Theory Comput.* **2011**, *7*, 525−537.
(42) Maier, J. A.; Martinez, C.; Kasavajhala, K.; Wickstrom, L.; Hauser, K. E.; Simmerling, C. ff14SB: Improving the Accuracy of Protein Side Chain and Backbone Parameters from ff99SB. *J. Chem. Theory Comput.* **2015**, *11*, 3696−3713.
(43) Jorgensen, W. L.; Chandrasekhar, J.; Madura, J. D.; Impey, R. W.; Klein, M. L. Comparison of Simple Potential Functions for Simulating Liquid Water. *J. Chem. Phys.* **1983**, *79*, 926−935.
(44) Joung, I. S.; Cheatham, T. E. Determination of Alkali and Halide Monovalent Ion Parameters for Use in Explicitly Solvated Biomolecular Simulations. *J. Phys. Chem. B* **2008**, *112*, 9020−9041.
(45) Li, P.; Roberts, B. P.; Chakravorty, D. K.; Merz, K. M. Rational Design of Particle Mesh Ewald Compatible Lennard-Jones Parameters for +2 Metal Cations in Explicit Solvent. *J. Chem. Theory Comput.* **2013**, *9*, 2733−2748.
(46) Wang, J.; Wolf, R. M.; Caldwell, J. W.; Kollman, P. A.; Case, D. A. Development and Testing of a General Amber Force Field. *J. Comput. Chem.* **2004**, *25*, 1157−1174.
(47) Bayly, C. I.; Cieplak, P.; Cornell, W.; Kollman, P. A. A Well-behaved Electrostatic Potential Based Method Using Charge Restraints for Deriving Atomic Charges: the RESP Model. *J. Phys. Chem.* **1993**, *97*, 10269−10280.
(48) Le Grand, S.; Götz, A. W.; Walker, R. C. SPFP: Speed without Compromise-A Mixed Precision Model for GPU Accelerated Molecular Dynamics Simulations. *Comput. Phys. Commun.* **2013**, *184*, 374−380.
(49) Salomon-Ferrer, R.; Case, D. A.; Walker, R. C. An Overview of the Amber Biomolecular Simulation Package. *Wiley Interdiscip. Rev.: Comput. Mol. Sci.* **2013**, *3*, 198−210.
(50) Darden, T.; York, D.; Pedersen, L. Particle Mesh Ewald: an N log(N) Method for Ewald Sums in Large Systems. *J. Chem. Phys.* **1993**, *98*, 10089−10092.
(51) Ryckaert, J.-P.; Ciccotti, G.; Berendsen, H. J. C. Numerical Integration of the Cartesian Equations of Motion of a System with Constraints: Molecular Dynamics of n-Alkanes. *J. Comput. Phys.* **1977**, *23*, 327−341.
(52) Rodriguez, A.; Laio, A. Clustering by Fast Search and Find of Density Peaks. *Science* **2014**, *344*, 1492−1496.
(53) Himo, F. Recent Trends in Quantum Chemical Modeling of Enzymatic Reactions. *J. Am. Chem. Soc.* **2017**, *139*, 6780−6786.
(54) Frisch, M. J.; Trucks, G. W.; Schlegel, H. B.; Scuseria, G. E.; Robb, M. A.; Cheeseman, J. R.; Scalmani, G.; Barone, V.; Petersson, G. A.; Nakatsuji, H.; Li, X.; Caricato, M.; Marenich, A. V.; Bloino, J.; Janesko, B. G.; Gomperts, R.; Mennucci, B.; Hratchian, H. P.; Ortiz, J. V.; Izmaylov, A. F.; Sonnenberg, J. L.; Williams-Young, D.; Ding, F.; Lipparini, F.; Egidi, F.; Goings, J.; Peng, B.; Petrone, A.; Henderson, T.; Ranasinghe, D.; Zakrzewski, V. G.; Gao, J.; Rega, N.; Zheng, G.; Liang, W.; Hada, M.; Ehara, M.; Toyota, K.; Fukuda, R.; Hasegawa, J.;


https://dx.doi.org/10.1021/acscatal.0c04148
*ACS Catal.* 2020, 10, 13825−13833

Ishida, M.; Nakajima, T.; Honda, Y.; Kitao, O.; Nakai, H.; Vreven, T.; Throssell, K.; Montgomery, J. A., Jr.; Peralta, J. E.; Ogliaro, F.; Bearpark, M. J.; Heyd, J. J.; Brothers, E. N.; Kudin, K. N.; Staroverov, V. N.; Keith, T. A.; Kobayashi, R.; Normand, J.; Raghavachari, K.; Rendell, A. P.; Burant, J. C.; Iyengar, S. S.; Tomasi, J.; Cossi, M.; Millam, J. M.; Klene, M.; Adamo, C.; Cammi, R.; Ochterski, J. W.; Martin, R. L.; Morokuma, K.; Farkas, O.; Foresman, J. B.; Fox, D. J. *Gaussian 16* Revision C.01; Gaussian, Inc.: Wallingford, CT, 2016.

(55) Francl, M. M.; Pietro, W. J.; Hehre, W. J.; Binkley, J. S.; Gordon, M. S.; DeFrees, D. J.; Pople, J. A. Self-consistent Molecular Orbital Methods. XXIII. A Polarization-type Basis Set for Second-row Elements. *J. Chem. Phys.* **1982**, *77*, 3654−3665.

(56) Gordon, M. S.; Binkley, J. S.; Pople, J. A.; Pietro, W. J.; Hehre, W. J. Self-consistent Molecular-orbital Methods. 22. Small Split-valence Basis Sets for Second-row Elements. *J. Am. Chem. Soc.* **1982**, *104*, 2797−2803.

(57) Marenich, A. V.; Cramer, C. J.; Truhlar, D. G. Universal Solvation Model Based on Solute Electron Density and on a Continuum Model of the Solvent Defined by the Bulk Dielectric Constant and Atomic Surface Tensions. *J. Phys. Chem. B* **2009**, *113*, 6378−6396.



https://dx.doi.org/10.1021/acscatal.0c04148
*ACS Catal.* 2020, 10, 13825−13833